

1
2
3
4
5
6
7
8
9
10
11
12
13
14
15
16
17
18

Atlantic Deep Water Formation Occurs Primarily in the Iceland Basin and Irminger Sea by Local Buoyancy Forcing

Tillys Petit¹, M. Susan Lozier¹, Simon A. Josey², Stuart A. Cunningham³

¹ School of Earth and Atmospheric Sciences, Georgia Institute of Technology, Atlanta, GA, USA

² National Oceanography Centre, Southampton, UK

³ Scottish Association for Marine Science, Oban, UK

Corresponding author: Tillys Petit (tillys.petit@gatech.edu)

Key Points:

- New observations reveal Atlantic Subpolar Gyre deep water is formed primarily in the Irminger and Iceland basins by local buoyancy forcing
- The deep water formed by buoyancy forcing in winter is not entirely exported the following months; a portion is stored in those basins
- The transformation and subsequent export of deep water southward are twice as large in winter 2014–2015 than in winter 2015–2016

19 Abstract

20 The Atlantic Meridional Overturning Circulation (AMOC), a key mechanism in the climate
21 system, delivers warm and salty waters from the subtropical gyre to the subpolar gyre and Nordic
22 Seas, where they are transformed into denser waters flowing southward in the lower AMOC
23 limb. The prevailing hypothesis is that dense waters formed in the Labrador and Nordic Seas are
24 the sources for the AMOC lower limb. However, recent observations reveal that convection in
25 the Labrador Sea contributes minimally to the total overturning of the subpolar gyre. In this
26 study, we show that the AMOC is instead primarily comprised of waters formed in the Nordic
27 Seas and Irminger and Iceland basins. A first direct estimate of heat and freshwater fluxes over
28 these basins demonstrates that buoyancy forcing during the winter months, can almost wholly
29 account for the dense waters of the subpolar North Atlantic that are exported as part of the
30 AMOC.

31

32 Plain Language Summary

33
34 The Atlantic Meridional Overturning Circulation (AMOC) is a key mechanism in the climate
35 system as it contributes to the uptake and storage of anthropogenic CO₂ in the deep ocean. As
36 global warming continues apace, climate scientists are concerned with the possibility of a
37 slowing AMOC due to changes in deep water formation at high latitudes in the North Atlantic.
38 Although wintertime conditions over the Labrador Sea have long been considered a strong
39 predictor of downstream AMOC change, recent results in the subpolar North Atlantic have
40 revealed that the volume of deep waters formed in the Labrador Sea is small compared with the
41 waters carried in the AMOC, creating an unresolved question as to the source of deep waters that
42 compose the lower AMOC limb. Here, we combine a collection of observations from the
43 subpolar gyre and Nordic Seas to show that the Iceland Basin and Irminger Sea are the main
44 sources for the lower limb. Additionally, we reveal that the production of deep waters can almost
45 entirely be accounted for by wintertime air-sea fluxes over those basins, and that some of the
46 dense waters formed via convection are stored in the Irminger and Iceland basins in subsequent
47 months.

48

49 **1 Introduction**

50 The Atlantic Meridional Overturning Circulation (AMOC) delivers warm and salty waters in its
51 upper limb to the North Atlantic subpolar gyre and Nordic Seas, where they are transformed into
52 large volumes of cold and fresh waters in the AMOC lower limb via air-sea buoyancy loss in
53 wintertime (Lozier, 2010). The prevailing hypothesis for the sources of the AMOC lower limb
54 has been that approximately half was provided by Nordic Sea waters flowing over the sills into
55 the Iceland and Irminger basins (Isachsen et al., 2007; Mauritzen, 1996), and half formed via
56 convection in the Labrador Sea (Bailey et al., 2005; Schmitz & McCartney, 1993; Worthington,
57 1976). However, results from a relatively new observational program have challenged that view
58 by providing evidence that the strength of Labrador Sea convection contributes minimally to the
59 total overturning of the subpolar gyre (Lozier et al., 2019). As such, the sources for waters of the
60 AMOC lower limb have come into question.

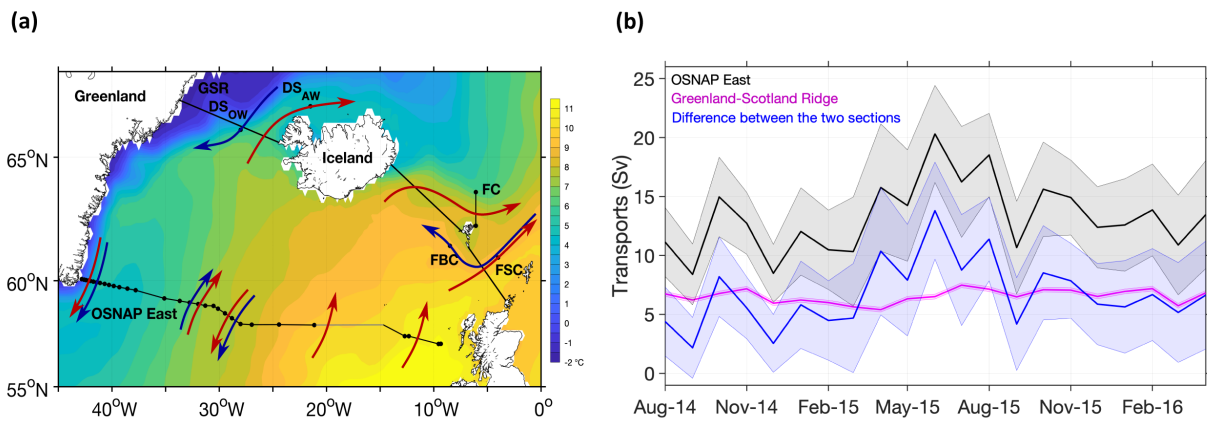
61 The Overturning in the Subpolar North Atlantic Program (OSNAP) array was deployed in the
62 summer of 2014 to provide continuous measurement of the AMOC at subpolar latitudes (Lozier
63 et al., 2017). The array is composed of two sections: OSNAP West at the Labrador Sea entrance,
64 and OSNAP East, which extends from the southeast tip of Greenland to the Scottish shelf
65 (Figure 1a). OSNAP observations through May 2016 (Lozier et al., 2019) show that the
66 overturning across OSNAP East (15.6 ± 0.8 Sv) exceeds the overturning across OSNAP West
67 (2.1 ± 0.3 Sv). A small overturning in the Labrador Sea was also estimated from composite
68 hydrographic sections during 1990–1997 (Pickart & Spall, 2007), suggesting that weak
69 overturning at OSNAP West is not an anomaly of the shorter OSNAP observational period.

70 To identify the source of the relatively large volume of the AMOC lower limb flowing across
71 OSNAP East (separated from the upper limb by the AMOC isopycnal, σ_{MOC} – section 2.1), we
72 compare continuous transport measurements across the Greenland-Scotland Ridge (GSR) with
73 those across OSNAP East (Figure 2). We find that the mean transport across GSR (-6.6 ± 0.4 Sv)
74 cannot explain that across OSNAP East (-13.2 ± 3.8 Sv), a result suggested by Sarafanov et al.
75 (2012) from an analysis of summer hydrographic sections. Similarly, waters flowing across GSR
76 in the AMOC upper limb (7.4 ± 0.4 Sv) are half of those flowing across OSNAP East
77 (15.0 ± 3.8 Sv). The overturning variability across OSNAP East can also not be attributed to the

78 deep waters flowing southward across GSR (Figure 1b) since the transport variability for the
 79 deep GSR waters (± 2 Sv) is small in comparison to that across OSNAP East (± 12 Sv).

80 Thus, the overall goal of this study is to ascertain the mechanism responsible for producing deep
 81 waters in the eastern subpolar North Atlantic. Specifically, we explore whether transformation of
 82 surface waters by air-sea fluxes of heat and freshwater in the region can account for the lower
 83 (upper) fluxes of 6.6 ± 3.8 Sv (7.6 ± 3.8 Sv) needed to close the mass budget between
 84 OSNAP East and GSR (Figure 2). To complement this exploration, we also assess the impact of
 85 buoyancy forcing over the Labrador and Nordic Seas during the OSNAP period.

86



87

88 **Figure 1. OSNAP East and GSR observations.** (a) Map of sea surface temperature ($^{\circ}$ C) during
 89 the OSNAP period showing mooring locations along OSNAP East and GSR for 1) Atlantic
 90 inflows at Denmark Strait (DS_{AW}), Faroe-Shetland Current (FSC) and Faroe-Current (FC) and 2)
 91 overflows at Denmark Strait (DS_{OW}) and Faroe-Bank Chanel (FBC). The grey line at
 92 OSNAP East denotes the glider survey region. Red and blue arrows depict upper and lower
 93 flows, respectively. (b) 30-day mean transports (positive southward) integrated over the lower
 94 layer at OSNAP East (black line) and GSR (magenta line), and their difference (blue line).
 95 Shading indicates uncertainty in the means. The two layers are separated by the 30-day varying
 96 isopycnal of the AMOC at OSNAP East, noted σ_{MOC} . See Methods for details on the uncertainty
 97 estimates.

98

99

100 2 Materials and Methods

101 2.1 The OSNAP East observations

102 The OSNAP East array consists of thirty-two moorings from the southeast tip of Greenland to
103 the Scottish shelf (Lozier et al., 2017). The distance between moorings (Figure 1) varies from
104 9.6 km at the Greenland shelf (42.5°W/60°N) to 389 km above the Hatton-Rockall Basins (14–
105 21°W/58°N). Geostrophic velocity fields are estimated from continuous temperature, salinity and
106 velocity measurements of the OSNAP moorings, combined with other observations (Argo
107 profiling floats, OSNAP gliders and CTD stations, WORLD Ocean Atlas 2013 climatology,
108 current meter velocities) for the period between August 2014 and May 2016. Salinity,
109 temperature and geostrophic velocity fields are gridded with a horizontal resolution of ~25 km
110 and a vertical resolution of 20 m (Li et al., 2017). Here, we used the gridded transports estimated
111 from the 30-day mean geostrophic velocities (Table S1).

112 The transports were integrated in the upper and lower layer at OSNAP East, which are separated
113 by the 30-day varying AMOC isopycnal, σ_{MOC} . The AMOC isopycnal is defined each month as
114 the density at the maximum of the overturning streamfunction in density space. It ranges from
115 27.38 kg m⁻³ in December 2014 to 27.76 kg m⁻³ in September 2014 with an average $\overline{\sigma_{\text{MOC}}}$ of
116 27.55 kg m⁻³.

117 Statistical uncertainties for the AMOC are estimated from Monte Carlo simulations (Thomson &
118 Emery, 2014), and were applied for the transports across OSNAP East. The statistical uncertainty
119 was estimated as 3.8 Sv for the upper and lower layers.

120 2.2 Exchanges across the Greenland-Scotland Ridge

121 We used transports across the GSR provided by the AtlantOS consortium (Bringedal et al.,
122 2018). The transports are estimated for the upper and lower layers from moorings and
123 hydrographic stations (Figure 1a). Note that the density limit between the layers is defined as
124 27.80 kg m⁻³ at the GSR.

125 The upper layer includes northward Atlantic water through the Denmark Strait (Jonsson &
126 Valdilarsson, 2012), the Faroe Current (Hansen et al., 2015) and the Faroe-Shetland Chanel
127 (Berx et al., 2013) (Figure 1a). Observations for this layer run through the period 1994–2014.

128 Because the transports do not span the entire OSNAP period, monthly averages were used to
129 create averaged time series for the rest of the OSNAP period. Indeed, we assume that the mean
130 states prevail through 2014–2016 as these flows are steady over time (Table S1).

131 The lower layer is composed of southward Denmark Strait Overflow Water (DSOW) at the
132 Denmark Strait (Jochumsen et al., 2017) and Iceland-Scotland Overflow Water (ISOW) at the
133 Faroe-Bank Channel (Hansen et al., 2016; Hansen & Østerhus, 2007) (Figure 1a). In that layer,
134 the averaged ISOW transports through the Wyville-Thomson Ridge and the Iceland-Faroe Ridge
135 of 0.8 Sv (Hansen et al., 2018) and 0.4 Sv (Sherwin, 2010), respectively, were included to the
136 exchanges through the Faroe-Bank Channel.

137 The standard error for the GSR transports is computed as: $E_{GSR} = \frac{std(T)}{\sqrt{n}}$; where $std(T)$ is the
138 standard deviation of the transports and n is the effective degree of freedom computed from the
139 autocorrelation function of the time series. Because the density limit between the upper and
140 lower layers, defined as 27.80 kg m^{-3} at the GSR, is denser than $\overline{\sigma_{MOC}} = 27.55 \text{ kg m}^{-3}$, an
141 uncertainty associated with the net mid-depth exchange across the GSR is added to the cross-
142 ridge flows (Sarafanov et al., 2012). The uncertainty in the sum of the upper and lower transports
143 is shared equally between the western and eastern sides of Iceland and applied to each cross-
144 ridge transport. The final error was estimated as 0.3 Sv for the southward DSOW and the
145 exchanges at the Faroe-Shetland Channel, and as 0.2 Sv for the southward ISOW and the
146 exchanges of Atlantic water through the Denmark Strait during the 21 months of OSNAP
147 observations.

148 2.3 Atmospheric Reanalysis

149 We use National Centers for Environmental Prediction (NCEP)/National Center for Atmospheric
150 Research (NCAR) atmospheric reanalysis (Kalnay et al., 1996) and European Centre for Medium
151 Range Weather Forecasts Reanalysis 5 (ERA5) atmospheric reanalysis (Poli et al., 2016) to
152 estimate air-sea heat and freshwater fluxes over the area defined between OSNAP East and GSR.
153 These are combined with monthly fields of subsurface salinity between August 2014 and
154 May 2016 to compute the transformations of outcropped waters. Subsurface salinities at 5-m
155 depth were derived from EN4.2.1 (Good et al., 2013) and, as for the NCEP/NCAR fluxes, were
156 subsampled onto the ERA5 grid of 30 km.

157 2.4 Transformation of outcropped waters

158 The transformation of surface water by air-sea fluxes is computed using a well-developed
 159 method based on a linearized version of the equation of state (Speer & Tziperman, 1992;
 160 Tziperman, 1986; Walin, 1982). Assuming steady state, the amount of water transformed across
 161 an isopycnal outcrop toward higher or lower densities by net heat and freshwater fluxes is
 162 computed for each month and each isopycnal σ following the equations below. A local surface
 163 density flux is integrated over time and the area of the density outcrop to yield the
 164 transformation, F (Figure S1). When σ does not outcrop in a given month, F is set to zero.

$$165 \quad F(\sigma^*) = \frac{1}{\Delta\sigma} \iint \left[-\frac{\alpha}{C_p} Q + \beta \frac{S}{1-S} (E - P) \right] \Pi(\sigma) dx dy$$

166 where

$$167 \quad \Pi(\sigma) = \begin{cases} 1 & \text{for } |\sigma - \sigma^*| \leq \frac{\Delta\sigma}{2} \\ 0 & \text{elsewhere} \end{cases}$$

168

169 α is the thermal expansion coefficient, β is the haline contraction coefficient, S is the subsurface
 170 salinity, C is the specific heat, H is the net heat flux into the ocean, E and P are the evaporation
 171 and precipitation, respectively. The bin size in density is set at $\Delta\sigma = 0.2 \text{ kg m}^{-3}$ to avoid noise at
 172 finer intervals (Speer & Tziperman, 1992).

173 Statistical uncertainty for the transformation is estimated as the standard error for the monthly
 174 transformations across σ_{MOC} : $Err = \frac{std(F\sigma)}{\sqrt{n}}$; where $std(F\sigma)$ is the standard deviation of the
 175 monthly transformations across σ_{MOC} over the 21 months of OSNAP observations, and n is the
 176 effective degree of freedom computed from the autocorrelation function of the time series. This
 177 error was estimated at 2.5 Sv in the Irminger Sea and Iceland Basin between OSNAP East and
 178 GSR.

179

180

181

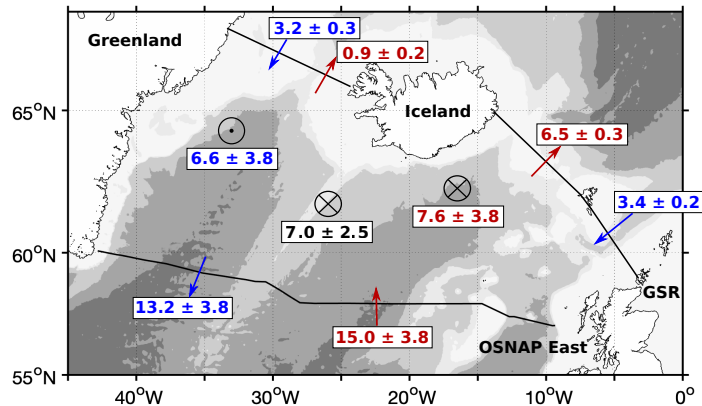
182

183 3 Results

184 3.1 Densification due to buoyancy forcing over the OSNAP period

185 The transport difference between deep flows across GSR and OSNAP East (6.6 ± 3.8 Sv;
186 Figure 2 and Table S1) is similar to that found (9.6 ± 3.5 Sv) using composites of summertime
187 hydrographic sections at GSR and at 59.5°N (Chafik & Rossby, 2019), the latter of which
188 roughly aligns with OSNAP East. In that study, the authors attribute the difference between the
189 volume of deep water coming over GSR and that exported at 59.5°N to entrainment and
190 subsequent densification of intermediate water by the overflow waters. Other studies highlight
191 buoyancy forcing, rather than entrainment, as the primary mechanism for densification in the
192 Irminger Sea (Brambilla et al., 2008; Brambilla & Talley, 2008), though a quantification of its
193 impact has yet to be made. That quantification is the focus of this section.

194 According to the method in Speer & Tziperman (1992) and described in section 2.4, we compute
195 the transformation of outcropped waters to densities exceeding σ_{MOC} , the AMOC isopycnal
196 separating the upper and lower limbs, during the 21 months of OSNAP data. Our estimate yields
197 a transformation of 7.0 ± 2.5 Sv over the area bounded by OSNAP East and GSR (Figure 2),
198 which matches remarkably well with the mean overturning estimated by the volume budget in
199 both layers (6.6 ± 3.8 Sv for the lower layer; 7.6 ± 3.8 Sv for the upper layer). Thus, the volume
200 of deep water exported from the Irminger and Iceland basins across OSNAP East can be
201 accounted for by overflow waters across the GSR and by water mass formation through
202 buoyancy loss over this region. The entrainment of ambient water by the overflow does not seem
203 to play a major role in the transformation of upper waters to densities larger than σ_{MOC} .
204 Nevertheless, the entrainment is not negligible in the subsequent transformation of the deep
205 waters within the lower limb of the AMOC (van Aken & de Jong, 2012; Dickson & Brown,
206 1994), and thus on the deep water properties exported southward.



207
 208 **Figure 2. Overturning and buoyancy forcing between OSNAP East and GSR.** Volume
 209 budget of the upper (red) and lower (blue) layers between GSR and OSNAP East (Sv). Within-
 210 layer transports are averaged over the OSNAP period. Circle with a central dot indicates the
 211 volume of water received in the lower layer from the upper layer estimated from the volume
 212 budget of the lower layer; circles with crosses indicate export of water from the upper layer to
 213 the lower layer estimated from the volume budget of the upper layer and from the averaged
 214 transformation across σ_{MOC} (black, unit Sv). Bathymetry is shaded for 500, 1000, 2000, 3000 m.
 215 Note that the red and blue arrows across the OSNAP line are placeholders for a number of
 216 significant currents that compose the upper and lower limbs.

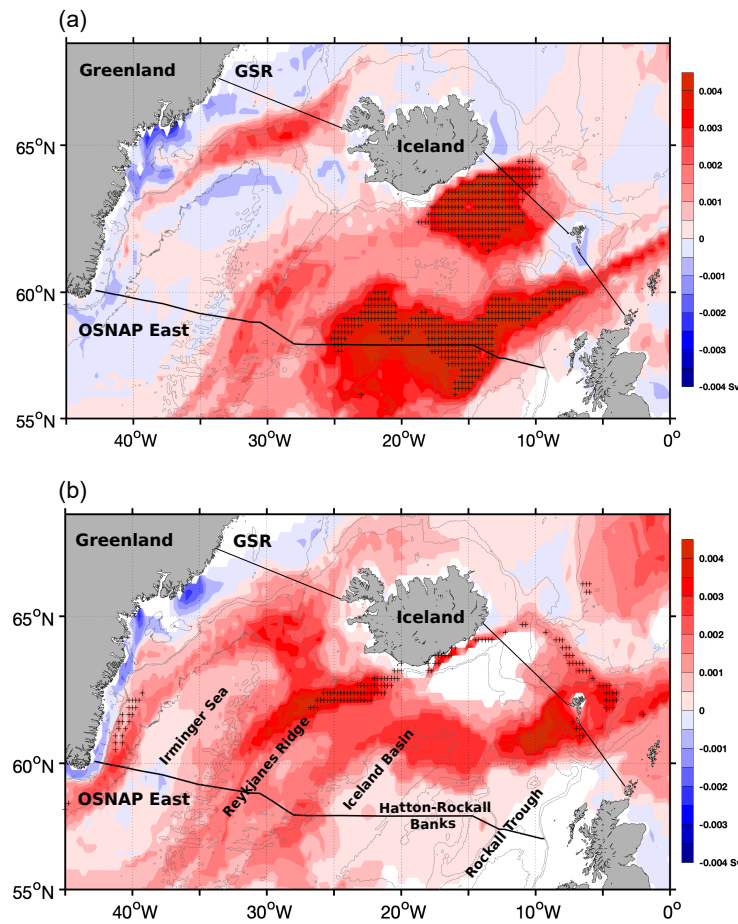
217
 218
 219 The strongest transformation of surface water to the mean AMOC density ($\overline{\sigma_{MOC}} = 27.55 \text{ kg m}^{-3}$)
 220 occurs along the boundary current in the Irminger Sea and north of 59°N in the region over the
 221 Reykjanes Ridge (Figure 3b), which is consistent with Brambilla et al. (2008). The importance of
 222 these areas for transformation is highlighted by the black crosses that denote regions where the
 223 27.55 kg m^{-3} isopycnal outcropped during all 8 months of the 2014–2015 and 2015–2016
 224 winters. With such persistent outcropping, these ‘hotspots’ play a key role in the transformation
 225 of light to dense waters between OSNAP East and GSR. In contrast, transformation is relatively
 226 weak over the Hatton-Rockall Basin and does not occur over the Rockall Trough at this density.
 227 However, the transformation to densities that define the lower AMOC limb is understood to be
 228 the final stage in water mass formation across the subpolar gyre. Thus, we also examine the

229 spatial pattern of transformation across 27.35 kg m^{-3} (Figure 3a), which we consider the density
230 of subpolar mode waters found in the eastern region of the subpolar gyre that are ‘pre-
231 conditioned’ to become the dense waters of the lower limb further downstream (Brambilla &
232 Talley, 2008; Talley & McCartney, 1982; Thierry et al., 2008). Strong transformation to this
233 density is found in the southeastern part of the Iceland Basin, whereas weak transformation is
234 observed over the Irminger Sea. Consistent with previous publications (Brambilla et al., 2008;
235 Desbruyères et al., 2019) our analysis shows that wintertime convection in the Iceland Basin,
236 Hatton-Rockall Basin and northern Rockall Trough provides critical preconditioning for the deep
237 waters of the AMOC lower limb.

238 We now extend our transformation analysis to the Labrador and Nordic Seas in order to
239 understand if estimates of overturning in those basins can similarly be explained by buoyancy
240 forcing. For the Labrador Sea, we find a water mass transformation of $1.5 \pm 0.7 \text{ Sv}$ to densities
241 exceeding 27.70 kg m^{-3} (Figure S1), the AMOC density at OSNAP West, which compares
242 reasonably well with the recently published estimate (Lozier et al., 2019) of overturning in that
243 basin of $2.1 \pm 0.3 \text{ Sv}$. Turning to the Nordic Seas, we have already noted that $6.6 \pm 0.4 \text{ Sv}$ of
244 overflow waters ($\sigma_0 > 27.80 \text{ kg m}^{-3}$) join the Irminger and Iceland basins through the GSR during
245 the OSNAP period. Our calculation of the transformation to densities greater than 27.80 kg m^{-3}
246 in the Nordic Seas (from GSR to Fram Strait and the Barents Sea Opening) during the same
247 period yields $4.7 \pm 1.5 \text{ Sv}$ (Figure S1), which agrees with the finding of Isachsen et al. (2007)
248 that the primary production of the dense water flowing across the GSR occurs in the Nordic
249 Seas. Thus, for all basins where we expect waters that comprise the deep limb of the AMOC to
250 be formed, we find that the volume of waters exported can largely be explained by buoyancy loss
251 over these basins in the winter months.

252 In earlier work using coupled models, a surface-forced overturning was estimated for the entire
253 North Atlantic north of a given latitude and compared against the model’s ‘actual’ overturning
254 computed using velocity fields (Grist et al., 2009; Josey et al., 2009). Josey et al. (2009) found
255 the surface-forced estimate was best matched to the actual by averaging the surface-forced
256 estimate over a number of years, e.g. 6 years at 60°N and 10 years at 45°N . Desbruyères et al.
257 (2019) found similar results using observations. In both studies, a lag is expected because of the
258 circulation time scales over a basin-wide area. In contrast, we focus here only on the Irminger

259 and Iceland basins and find that local surface fluxes are driving the diapycnal fluxes with little or
 260 no lag.



261
 262 **Figure 3. Spatial pattern of transformation.** Transformation (Sv) at (a) 27.35 kg m^{-3} and (b)
 263 27.55 kg m^{-3} over the Irminger Sea and Iceland Basin averaged over the 21-month OSNAP
 264 period and derived from the heat and freshwater fluxes of ERA5 and NCEP. Positive
 265 transformation are associated with densification to the denoted isopycnals. Black crosses indicate
 266 outcropping areas of the isopycnals during all eight months of winter (December–March) 2014–
 267 2015 and 2015–2016. Bathymetry contours are at 500, 1,000 m, 2,500 m. White indicates
 268 regions with no outcropping in any month. In addition to the Irminger Sea boundary and
 269 Reykjanes Ridge, a region of strong transformation is centered on $(62^\circ\text{N}, 10^\circ\text{W})$, however it is
 270 not associated with persistent outcropping during all eight months of winter 2014–2015.
 271

272 3.2 Temporal variability of the overturning in the Iceland and Irminger basins

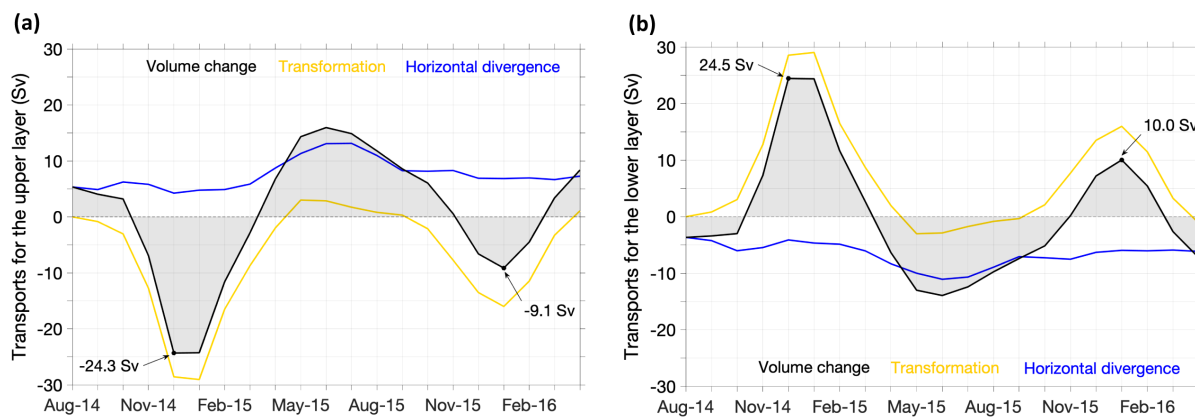
273 Over the 21 months of OSNAP observations, overturning variability between OSNAP East and
274 GSR is large, with the 30-day means ranging from 2.2 ± 2.6 Sv in September 2014 to
275 13.8 ± 4.1 Sv in June 2015 (Figure 1b). To further investigate this variability, the volume change
276 for the upper and lower layers for each month is estimated by adding the net volume gain/loss
277 due to horizontal advection and the net volume gain/loss due to transformation into/out of that
278 layer.

279 Volume changes for the lower layer can be described with two steps: accumulation of water from
280 the upper layer in winter due to densification, and then subsequent export of water out of the
281 Irminger and Iceland basins the following months (Figure 4). In winter 2014–2015, the
282 transformation of water to densities greater than σ_{MOC} reaches a total of 29.1 Sv in January of
283 2015. During those winter months, the loss of water out of the lower layer is steady, but weak,
284 with a minimum of -4.3 Sv in December 2014, thus the layer thickens. For the upper layer, the
285 strong densification due to buoyancy forcing overwhelms the weak advective gain such that
286 there is a thinning of the layer during those months. Note that the thinning (volume loss) and
287 thickening (volume gain) for the upper and lower layers, respectively, are in close agreement,
288 with extrema in December 2014 of -24.3 Sv for the upper layer and of 24.5 Sv for the lower
289 layer.

290 After January 2015, transformation to densities greater than σ_{MOC} weakens while the net volume
291 exported out of the basins due to advection for the lower layer reaches its maximum of -11.1 Sv
292 in July 2015. Thus, the lower layer thins during spring to summer.

293 The maximum volume of water exported out of the lower layer by the horizontal flow field lags
294 the peak of densification by five months. The length of this delay — between the formation of
295 dense water and its export to the boundary current in a marginal sea, such as the Irminger Sea —
296 is consistent with modeling studies that attribute the exchange between the convective region and
297 the boundary current to an eddy transport mechanism (Brüggemann & Katsman, 2019; Sayol et
298 al., 2019). The delay depends upon the location of the convection and ranges from three months
299 if convection takes place along the Irminger Current to more than twelve months if it is in the
300 interior of the Irminger Sea (Le Bras et al., 2020).

301 Over one year, the volume gain in the lower layer due to transformation exceeds the volume lost
 302 due to advection, implying that a fraction of the transformed water is stored in the Irminger and
 303 Iceland basins and not exported seasonally. From October 2014 to September 2015, 4.5 Sv is
 304 stored in the lower layer of these basins. We note that the volume accumulated in the lower layer
 305 varies from year to year (Figure 4): the accumulation is larger in winter 2014–2015 (24.5/-
 306 24.3 Sv) than in winter 2015–2016 (10.0/-9.1 Sv). Thus, the overturning variability downstream
 307 is impacted by the advection of dense water exported across OSNAP East as much as by the
 308 transformation. On longer times scales, we have an expectation that the export of waters out of
 309 the lower limb will match the transformation, or production, of the dense waters in that limb.



310
 311 **Figure 4. Monthly variability of the layer volumes.** 30-day mean volume change (Sv) in the
 312 (a) upper and (b) lower layers between OSNAP East and GSR (black lines). The volume change
 313 is estimated by combining the transformation at the AMOC isopycnal through air-sea flux
 314 forcing (Sv, yellow lines) and the horizontal divergence of transport into each layer as estimated
 315 in Figure 1b (Sv, blue lines). The three variables are positive for inflows into the layer, such that
 316 positive transformations are associated with lightening in the upper layer and densification in the
 317 lower layer. Positive shading indicates an accumulated volume in the layer and negative shading
 318 indicates a volume lost for the layer. The products are smoothed over three months. The two
 319 layers are separated by the 30-day varying isopycnal of the AMOC at OSNAP East, σ_{MOC} , which
 320 has an average of 27.55 kg m^{-3} .

321

322 **4 Conclusion and implications**

323 From the first synthesis of in situ observations (OSNAP and NAACLIM) and air-sea buoyancy
324 exchanges in each basin of the subpolar North Atlantic and the Nordic Seas, a new understanding
325 of overturning in the eastern subpolar gyre emerges. The sources for the AMOC lower limb deep
326 water are, in order of importance, the Irminger and Iceland basins, the Nordic Seas, and finally
327 the Labrador Sea. This relevance stands in contrast to past studies that partitioned the deep water
328 sources between the Nordic and Labrador Seas. We suggest that this earlier partitioning resulted
329 from the fact that part of the deep waters formed in the Irminger and Iceland basins are carried
330 toward the Labrador Sea via the Deep Western Boundary Current. Then, although they are
331 further modified in the Labrador Sea and exit the basin as ‘Labrador Sea Water’, the bulk of
332 these waters joined the lower limb of the AMOC upstream.

333 Our results reveal that the production of deep water in the Irminger and Iceland basins can
334 almost entirely be accounted for by buoyancy forcing over those basins. The close agreement
335 between overturning and buoyancy forcing over the subpolar gyre highlights the key role of air-
336 sea fluxes in establishing the state of the AMOC. Furthermore, considering the relatively large
337 fraction of transformed water that is stored in the Irminger and Iceland basins each year, an
338 investigation into the sensitivity of the AMOC to previously observed intense interannual
339 variability in this region (Josey et al., 2019; Josey et al., 2018) is warranted.

340

341 **References**

342 van Aken, H. M., & de Jong, M. F. (2012). Hydrographic variability of Denmark Strait Overflow
343 Water near Cape Farewell with multi-decadal to weekly time scales. *Deep-Sea Research*
344 *Part I: Oceanographic Research Papers*, 66, 41–50.
345 <https://doi.org/10.1016/j.dsr.2012.04.004>

346 Bailey, D. A., Rhines, P. B., & Häkkinen, S. (2005). Formation and pathways of North Atlantic
347 Deep Water in a coupled ice–ocean model of the Arctic–North Atlantic Oceans. *Climate*
348 *Dynamics*, 25(5), 497–516. <https://doi.org/10.1007/s00382-005-0050-3>

349 Berx, B., Hansen, B., Østerhus, S., Larsen, K. M., Sherwin, T., & Jochumsen, K. (2013).

- 350 Combining in situ measurements and altimetry to estimate volume, heat and salt transport
351 variability through the Faroe-Shetland Channel. *Ocean Science*, 9(4), 639–654.
352 <https://doi.org/10.5194/os-9-639-2013>
- 353 Brambilla, E., & Talley, L. D. (2008). Subpolar mode water in the northeastern Atlantic: 1.
354 Averaged properties and mean circulation. *Journal of Geophysical Research: Oceans*,
355 113(4), 1–16. <https://doi.org/10.1029/2006JC004062>
- 356 Brambilla, E., Talley, L. D., & Robbins, P. E. (2008). Subpolar Mode Water in the northeastern
357 Atlantic: 2. Origin and transformation. *Journal of Geophysical Research*, 113(C4), C04026.
358 <https://doi.org/10.1029/2006JC004063>
- 359 Le Bras, I. A. -A., Straneo, F., Holte, J., Jong, M. F., & Holliday, N. P. (2020). Rapid Export of
360 Waters Formed by Convection Near the Irminger Sea’s Western Boundary. *Geophysical*
361 *Research Letters*, 47(3). <https://doi.org/10.1029/2019gl085989>
- 362 Bringedal, C., Eldevik, T., Skagseth, Ø., Spall, M. A., & Østerhus, S. (2018). Structure and
363 forcing of observed exchanges across the Greenland-Scotland Ridge. *Journal of Climate*,
364 31(24), 9881–9901. <https://doi.org/10.1175/JCLI-D-17-0889.1>
- 365 Brüggemann, N., & Katsman, C. A. (2019). Dynamics of downwelling in an eddying marginal
366 sea: contrasting the Eulerian and the isopycnal perspective. *Journal of Physical*
367 *Oceanography*, 3017–3035. <https://doi.org/10.1175/jpo-d-19-0090.1>
- 368 Chafik, L., & Rossby, T. (2019). Volume, Heat, and Freshwater Divergences in the Subpolar
369 North Atlantic Suggest the Nordic Seas as Key to the State of the Meridional Overturning
370 Circulation. *Geophysical Research Letters*, 46(9), 4799–4808.
371 <https://doi.org/10.1029/2019GL082110>
- 372 Desbruyères, D. G., Mercier, H., Maze, G., & Daniault, N. (2019). Surface predictor of
373 overturning circulation and heat content change in the subpolar North Atlantic. *Ocean*
374 *Science*, 15(3), 809–817. <https://doi.org/10.5194/os-15-809-2019>
- 375 Dickson, R., & Brown, J. (1994). The production of North Atlantic Deep Water : Sources , rates ,
376 and pathways la . Worthington ’ s scheme conversion paths North Circled numbers are

- 377 transport estimates in Sverdrups , where $1b$. The recasting of Worthington ' s scheme by
378 McCartney and. *Journal of Geophysical Research*, 99(94), 12,319-12,341.
- 379 Good, S. A., Martin, M. J., & Rayner, N. A. (2013). EN4: Quality controlled ocean temperature
380 and salinity profiles and monthly objective analyses with uncertainty estimates. *Journal of*
381 *Geophysical Research: Oceans*, 118(12), 6704–6716.
382 <https://doi.org/10.1002/2013JC009067>
- 383 Grist, J. P., Marsh, R., & Josey, S. A. (2009). On the relationship between the north Atlantic
384 meridional overturning circulation and the surface-forced overturning streamfunction.
385 *Journal of Climate*, 22(19), 4989–5002. <https://doi.org/10.1175/2009JCLI2574.1>
- 386 Hansen, B., Larsen, K. M. H., Hátún, H., Kristiansen, R., Mortensen, E., & Østerhus, S. (2015).
387 Transport of volume, heat, and salt towards the Arctic in the Faroe Current 1993-2013.
388 *Ocean Science*, 11(5), 743–757. <https://doi.org/10.5194/os-11-743-2015>
- 389 Hansen, Bogi, & Østerhus, S. (2007). Faroe Bank Channel overflow 1995-2005. *Progress in*
390 *Oceanography*, 75(4), 817–856. <https://doi.org/10.1016/j.pocean.2007.09.004>
- 391 Hansen, Bogi, Husgaro, K. M., Hátún, H., & Østerhus, S. (2016). A stable Faroe Bank Channel
392 overflow 1995-2015. *Ocean Science*, 12(6), 1205–1220. [https://doi.org/10.5194/os-12-](https://doi.org/10.5194/os-12-1205-2016)
393 1205-2016
- 394 Hansen, Bogi, Margretha Húsgar Larsen, K., Malskær Olsen, S., Quadfasel, D., Jochumsen, K.,
395 & Østerhus, S. (2018). Overflow of cold water across the Iceland-Faroe Ridge through the
396 Western Valley. *Ocean Science*, 14(4), 871–885. <https://doi.org/10.5194/os-14-871-2018>
- 397 Isachsen, P. E., Mauritzen, C., & Svendsen, H. (2007). Dense water formation in the Nordic Seas
398 diagnosed from sea surface buoyancy fluxes. *Deep-Sea Research Part I: Oceanographic*
399 *Research Papers*, 54(1), 22–41. <https://doi.org/10.1016/j.dsr.2006.09.008>
- 400 Jochumsen, K., Moritz, M., Nunes, N., Quadfasel, D., Larsen, K. M. H., Hansen, B., et al.
401 (2017). Revised transport estimates of the Denmark Strait overflow. *Journal of Geophysical*
402 *Research: Oceans*, 122(4), 3434–3450. <https://doi.org/10.1002/2017JC012803>
- 403 Jonsson, S., & Valdilarsson, H. (2012). Water mass transport variability to the North Icelandic

- 404 shelf, 1994-2010. *ICES Journal of Marine Science*, 69(5), 809–815.
405 <https://doi.org/doi:10.1093/icesjms/fss024>
- 406 Josey, S. A., de Jong, M. F., Oltmanns, M., Moore, G. K., & Weller, R. A. (2019). Extreme
407 Variability in Irminger Sea Winter Heat Loss Revealed by Ocean Observatories Initiative
408 Mooring and the ERA5 Reanalysis. *Geophysical Research Letters*, 46(1), 293–302.
409 <https://doi.org/10.1029/2018GL080956>
- 410 Josey, Simon A., Grist, J. P., & Marsh, R. (2009). Estimates of meridional overturning
411 circulation variability in the North Atlantic from surface density flux fields. *Journal of*
412 *Geophysical Research: Oceans*, 114(9), 1–11. <https://doi.org/10.1029/2008JC005230>
- 413 Josey, Simon A., Hirschi, J. J.-M., Sinha, B., Duchez, A., Grist, J. P., & Marsh, R. (2018). The
414 Recent Atlantic Cold Anomaly: Causes, Consequences, and Related Phenomena. *Annual*
415 *Review of Marine Science*, 10(1), 475–501. [https://doi.org/10.1146/annurev-marine-](https://doi.org/10.1146/annurev-marine-121916-063102)
416 [121916-063102](https://doi.org/10.1146/annurev-marine-121916-063102)
- 417 Kalnay, E., Kanamitsu, M., Kistler, R., Collins, W., Deaven, D., Gandin, L., et al. (1996). The
418 NCEP/NCAR 40-year reanalysis project. *Bulletin of the American Meteorological Society*.
419 [https://doi.org/10.1175/1520-0477\(1996\)077<0437:TNYRP>2.0.CO;2](https://doi.org/10.1175/1520-0477(1996)077<0437:TNYRP>2.0.CO;2)
- 420 Li, F., Lozier, M. S., & Johns, W. E. (2017). Calculating the meridional volume, heat, and
421 freshwater transports from an observing system in the subpolar North Atlantic: Observing
422 system simulation experiment. *Journal of Atmospheric and Oceanic Technology*, 34(7),
423 1483–1500. <https://doi.org/10.1175/JTECH-D-16-0247.1>
- 424 Lozier, M. S., Li, F., Bacon, S., Bahr, F., Bower, A. S., Cunningham, S. A., et al. (2019). A sea
425 change in our view of overturning in the subpolar North Atlantic. *Science*, 363(6426), 516–
426 521. <https://doi.org/10.1126/science.aau6592>
- 427 Lozier, M. Susan. (2010). Deconstructing the conveyor belt. *Science*, 328(5985), 1507–1511.
428 <https://doi.org/10.1126/science.1189250>
- 429 Lozier, M. Susan, Bacon, S., Bower, A. S., Cunningham, S. A., De Jong, M. F., De Steur, L., et
430 al. (2017). Overturning in the Subpolar north Atlantic program: A new international ocean

- 431 observing system. *Bulletin of the American Meteorological Society*, 98(4), 737–752.
432 <https://doi.org/10.1175/BAMS-D-16-0057.1>
- 433 Mauritzen, C. (1996). Production of dense overflow waters feeding the North Atlantic across the
434 Greenland-Scotland Ridge. Part 1: Evidence for a revised circulation scheme. *Deep-Sea
435 Research Part I: Oceanographic Research Papers*, 43(6), 769–806.
436 [https://doi.org/10.1016/0967-0637\(96\)00037-4](https://doi.org/10.1016/0967-0637(96)00037-4)
- 437 Pickart, R. S., & Spall, M. A. (2007). Impact of Labrador Sea Convection on the North Atlantic
438 Meridional Overturning Circulation. *Journal of Physical Oceanography*, 37(9), 2207–2227.
439 <https://doi.org/10.1175/jpo3178.1>
- 440 Poli, P., Hersbach, H., Dee, D. P., Berrisford, P., Simmons, A. J., Vitart, F., et al. (2016). ERA-
441 20C: An atmospheric reanalysis of the twentieth century. *Journal of Climate*, 29(11), 4083–
442 4097. <https://doi.org/10.1175/JCLI-D-15-0556.1>
- 443 Sarafanov, A., Falina, A., Mercier, H., Sokov, A., Lherminier, P., Gourcuff, C., et al. (2012).
444 Mean full-depth summer circulation and transports at the northern periphery of the Atlantic
445 Ocean in the 2000s. *Journal of Geophysical Research: Oceans*, 117(1), C01014.
446 <https://doi.org/10.1029/2011JC007572>
- 447 Sayol, J.-M., Dijkstra, H., & Katsman, C. (2019). Seasonal and regional variations of sinking in
448 the subpolar North Atlantic from a high-resolution ocean model. *Ocean Science
449 Discussions*, (April), 1–31. <https://doi.org/10.5194/os-2019-27>
- 450 Schmitz, W. J., & McCartney, M. S. (1993). On the North Atlantic Circulation. *Reviews of
451 Geophysics*, 31(1), 29–49. <https://doi.org/10.1029/92RG02583>
- 452 Sherwin, T. J. (2010). Observations of the velocity profile of a fast and deep oceanic density
453 current constrained in a gully. *Journal of Geophysical Research: Oceans*, 115(3), 1–14.
454 <https://doi.org/10.1029/2009JC005557>
- 455 Speer, K., & Tziperman, E. (1992). Rates of water mass formation in the North Atlantic ocean.
456 *Journal of Physical Oceanography*, 22(1), 93–104.
- 457 Talley, L. D., & McCartney, M. S. (1982). Distribution and Circulation of Labrador Sea Water.

458 *Journal of Physical Oceanography*. [https://doi.org/10.1175/1520-](https://doi.org/10.1175/1520-0485(1982)012<1189:DACOLS>2.0.CO;2)
459 [0485\(1982\)012<1189:DACOLS>2.0.CO;2](https://doi.org/10.1175/1520-0485(1982)012<1189:DACOLS>2.0.CO;2)

460 Thierry, V., de Boisséon, E., & Mercier, H. (2008). Interannual variability of the Subpolar Mode
461 Water properties over the Reykjanes Ridge during 1990-2006. *Journal of Geophysical*
462 *Research: Oceans*, 113(4), C04016. <https://doi.org/10.1029/2007JC004443>

463 Thomson, R. E., & Emery, W. J. (2014). *Data Analysis Method in Physical Oceanography*
464 (Elsevier S).

465 Tziperman, E. (1986). On the role of interior mixing and air-sea fluxes in determining the
466 stratification and circulation of the oceans. *Journal of Physical Oceanography*.
467 [https://doi.org/10.1175/1520-0485\(1986\)016<0680:OTROIM>2.0.CO;2](https://doi.org/10.1175/1520-0485(1986)016<0680:OTROIM>2.0.CO;2)

468 Walin, G. (1982). On the relation between sea-surface heat flow and thermal circulation in the
469 ocean. *Tellus*, 34, 187–195.

470 Worthington, L. V. (1976). On the North Atlantic circulation. *The Johns Hopkins Oceanogr.*
471 *Stud.*, 6, 110.

472

473 **Acknowledgments**

474 **Funding:** T.P. and M.S.L. acknowledge support from the Physical Oceanography Program of
475 the US National Science Foundation (Grant 3331843). S.A.J. acknowledges funding from the
476 UK Natural Environment Research Council, including the North Atlantic Climate System
477 Integrated Study program (reference number NE/N018044/1). S.C.U. was supported by UK
478 NERC National Capability programme the Extended Ellett Line and CLASS (NE/R015953/1),
479 and NERC Large Grant UK OSNAP (NE/K010875/1) and from the European Union's Horizon
480 2020 research and innovation programme under grant agreement No 678760 (ATLAS) and No
481 727852 (Blue-Action). This output reflects only the author's view and the European Union
482 cannot be held responsible for any use that may be made of the information contained therein.

483 **Competing interests:** The authors declare no competing interests. **Data and materials**

484 **availability:** The data used for the conclusion of the paper are archived in data repositories.

485 Observations at the OSNAP East section are accessible at <https://www.o->
486 [snap.org/observations/data/](https://www.o-snap.org/observations/data/) and those at the Greenland-Scotland Ridge are provided by Atlantos
487 (<http://www.oceansites.org/tma/gsr.html>). The atmospheric reanalyses are freely available
488 through <https://www.ecmwf.int/en/forecasts/datasets/reanalysis-datasets/era5> and
489 <https://www.ncep.noaa.gov>. The subsurface salinities derived from EN4.2.1 are accessible at
490 https://www.metoffice.gov.uk/hadobs/en4/download-en4-2-1.html#l09_profiles.